Mon. Not. R. Astron. Soc. **000**, ??–?? (0000) Printed 12 August 2002 (MN LATEX style file v1.4)

The Large Scale Distribution of Neutral Hydrogen in the Fornax Region

Meryl Waugh[1], M.J. Drinkwater[1], R.L. Webster[1], L. Staveley-Smith[2], V.A. Kilborn[3], D.G. Barnes[4], R. Bhathal[5], W.J.G. de Blok[2], P.J. Boyce[6], M.J. Disney[6], R.D. Ekers[2], K.C. Freeman[7], B.K. Gibson[4], P.A. Henning[8], H. Jerjen[7], P.M. Knezek[9], B. Koribalski[2], M. Marquarding[2], R.F. Minchin[6], R.M. Price[8], M.E. Putman[10], S.D. Ryder[11], E.M. Sadler[12], F. Stootman[5] and M.A. Zwaan[1]

[1] *School of Physics, University of Melbourne, VIC 3010, Australia*
[2] *Australia Telescope National Facility, CSIRO, P.O. Box 76, Epping, NSW 1710, Australia*
[3] *University of Manchester, Jodrell Bank Observatory, Macclesfield, Cheshire, UK, SKll 9DL*
[4] *Centre for Astrophysics & Supercomputing, Swinburne University, Mail #31, P.O. Box 218, Hawthorn, VIC 3122, Australia*
[5] *University of Western Sydney Macarthur, Department of Physics, P.O. Box 555, Campbelltown, NSW 2560, Australia*
[6] *University of Wales, Cardiff, Department of Physics & Astronomy, P.O. Box 913, Cardiff CF2 3YB, U.K.*
[7] *Research School of Astronomy and Astrophysics, ANU, Weston Creek P.O., Weston, ACT 2611, Australia*
[8] *University of New Mexico, Department of Physics & Astronomy, 800 Yale Blvd. NE, Albuquerque, NM 87131, USA*
[9] *Space Telescope Science Institute, 3700 San Martin Drive, Baltimore, MD, 21218, USA*
[10] *Center for Astrophysics and Space Astronomy, University of Colorado, Boulder, CO 80309-0389, USA. Hubble Fellow*
[11] *Anglo-Australian Observatory, P.O. Box 296, Epping, NSW 1710, Australia*
[12] *University of Sydney, Astrophysics Department, School of Physics, A28, Sydney, NSW 2006, Australia*

Accepted 0000 Month 00. Received 0000 Month 00

ABSTRACT

Using data from the HI Parkes All Sky Survey (HIPASS), we have searched for neutral hydrogen in galaxies in a region $\sim 25^\circ \times 25^\circ$ centred on NGC 1399, the nominal centre of the Fornax Cluster. Within a velocity search range of 300–3700 km s^{-1} and to a 3σ lower flux limit of $\sim$40 mJy, 110 galaxies with HI emission were detected, one of which is previously uncatalogued. None of the detections has early-type morphology. Previously unknown velocities for 14 galaxies have been determined, with a further 4 velocity measurements being significantly dissimilar to published values. Identification of an optical counterpart is relatively unambiguous for more than $\sim$90% of our HI galaxies. The galaxies appear to be embedded in a sheet at the cluster velocity which extends for more than 30° across the search area. At the nominal cluster distance of $\sim$20 Mpc, this corresponds to an elongated structure more than 10 Mpc in extent. A velocity gradient across the structure is detected, with radial velocities increasing by $\sim$500 km s^{-1} from SE to NW. The clustering of galaxies evident in optical surveys is only weakly suggested in the spatial distribution of our HI detections. Of 62 HI detections within a 10° projected radius of the cluster centre, only two are within the core region (projected radius $<1^\circ$) and less than 30% are within 3.5°, suggesting a considerable deficit of HI-rich galaxies in the centre of the cluster. However, relative to the field, there is a $3(\pm 1)$-fold excess of HI-rich galaxies in the outer parts of the cluster where galaxies may be infalling towards the cluster for the first time.

Key words: Surveys – Galaxies:clusters:individual:Fornax – Galaxies:evolution – Large-scale Structure of Universe – Radio lines:galaxies

1 INTRODUCTION — THE FORNAX CLUSTER

The Fornax Cluster is amongst the closest and most well studied clusters in the southern sky, providing an interesting nearby field for the study of large scale structure (LSS), galaxy populations, dynamics and evolution in the cluster environment. Although the cluster is not as rich as other well-studied clusters, its core galaxy density is relatively high (Ferguson 1989a).

The central galaxy of the Fornax Cluster is the giant elliptical NGC 1399 with a radial velocity of $\sim$1425 km s^{-1} . Its position (R.A. $3^h38^m29^s.3$, Dec. $-35°27'01''$ [J2000]) is generally adopted as the approximate centre of the cluster. Also particularly well-studied are the barred spiral NGC 1365 and the strong radio continuum source NGC 1316 (Fornax A). Although the Cepheid distances to three Fornax spirals have been determined (NGC 1365 at 18.6 ± 0.6 Mpc , NGC 1326A at 18.7 ± 2.0 Mpc and NGC 1425 at 22.2 ± 2.7 Mpc) (Madore et al. 1999, Prosser et al. 1999 and Mould et al. 2000, respectively), an accurate cluster distance is still somewhat uncertain, particularly in the light of the substructure analysis of Drinkwater et al. (2001a). In this paper, we adopt a value close to the mean of the three Cepheid estimates, 20 Mpc, as the cluster distance.

Recessional velocities of Fornax Cluster galaxies range from about 700 to 2200 km s^{-1} (Drinkwater et al. 2001b). No galaxies have been detected, either optically or in HI, in front of the cluster and few in the void behind it, in the region 2200–4500 km s^{-1} . Galaxies beyond about $cz = 3000$ km s^{-1} would not be classified as likely cluster members.

Covering an area of nearly 40 deg^2, Ferguson's optical Fornax Cluster Catalogue (FCC) (Ferguson 1989b) identified 340 likely cluster members, only 85 of which had published redshifts. Subsequent surveys have reassigned some members from likely membership to background status and *vice versa* and have also determined some previously unknown redshifts (e.g. Drinkwater et al. 2001b, Schröder, Drinkwater & Richter 2001, Drinkwater & Gregg 1998).

Drinkwater et al. (2001b) have recently measured the redshifts of more than 500 bright galaxies ($16.5 < B_J < 18$) in a $6°\times6°$ field centred on Fornax and using the FLAIR-II spectrograph on the UK Schmidt Telescope. A deeper unbiased Fornax Cluster Spectroscopic Survey (FCSS) is targetting *all* objects ($\sim$ 14000) within the magnitude limits $16.5 \leq B_J \leq 19.7$ in four π deg^2 fields (total area $\sim$12 deg^2), utilising the 2 degree Field (2dF) spectrograph of the Anglo-Australian Telescope (Drinkwater et al. 2000).

Several pointed neutral hydrogen surveys of Fornax galaxies have been reported (e.g. Schröder et al. 2001, Bureau, Mould & Staveley-Smith 1996). The first blind HI survey of Fornax was conducted by Barnes et al. (1997) and covered about $8°\times8°$ of the central cluster region. We report here on a larger, deeper, blind survey of the region, with detection rates about three times greater.

Utilising the 13-beam receiver on the Parkes 64 m radio telescope, the HI Parkes All Sky Survey (HIPASS) covered the entire southern sky south of $\delta = 2°$ for λ 21cm neutral hydrogen (Staveley-Smith et al. 1996). Observations were completed in March 2000 and this ambitious project has enormous scientific potential, providing a wealth of new HI data, unbiased by optical selection criteria or effects. For this paper, we sampled about 3% of the HIPASS dataset (13 of 388 cubes) to examine the distribution, number density and HI content of galaxies over a $25°\times25°$ field centred on the Fornax Cluster but extending well beyond it. Our results contribute new information pertaining to galaxy evolution and dynamics and the large scale structure (LSS) of the local universe in the Fornax region.

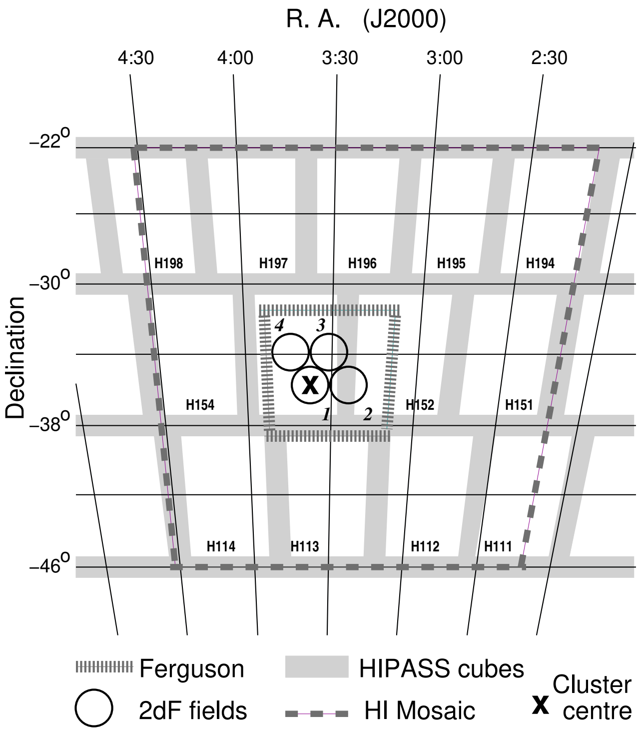

Figure 1. Relative positions and approximate sizes of various optical and HI surveys in the Fornax region. The Ferguson Cluster Catalog region is indicated by the thin dashed lines, the 2dF survey fields are shown as circles and the approximate positions of standard HIPASS cubes are outlined. The area covered by our Fornax HI mosaic is indicated by heavy dashed lines. The cross shows the position of NGC 1399 at the cluster centre.

The fields covered by several surveys of the Fornax cluster are illustrated in Fig. ??. Also shown are the positions of the 13 HIPASS cubes used to compile our mosaic.

Further details and parameters of HIPASS are outlined in Section ??. Galaxies were detected and confirmed in the mosaic by the methods described in Section ??. The properties of the galaxies are examined in Section ?? and the results of this study are summarised in Section ??.

2 DATA SAMPLE

The characteristics of the Parkes multibeam system used for HIPASS are described by Staveley-Smith et al. (1996). Barnes et al. (2001) have comprehensively detailed the survey observing parameters, data collection, calibration and imaging techniques. For the survey, the telescope scanned in declination strips of 8°, each 1.7° wide. The scanning procedure was optimized to ensure approximately uniform sky coverage at full sensitivity whilst still allowing online data processing to be automated and statistically robust. The mean beamwidth is 14.3 arcmin (FWHM) and the total integration time is 460 s beam^{-1}. After median gridding, data were processed into cubes measuring $8°\times8°$ on the sky, with overlap of up to $\sim$1°. Pixel size is 4 arcminutes. The survey has a bandwidth of 64 MHz, detecting HI emission in the range $-1280 < cz < 12700$ km s^{-1} over 1024 planes at a separation of 13.2 km s^{-1}. The velocity resolution after smoothing is 18 km s^{-1}.

The final HIPASS data have an RMS noise level of around 13.3 mJy and thus a 3σ detection limit of $\sim$40 mJy beam^{-1}. The gridded HIPASS beam has a FWHM of 15.5 arcmin and an image pixel size of 4 arcmin. Most sources in our mosaic survey are essentially unresolved and a final positional accuracy of 3–4$'$ is expected, depending on the flux (Barnes 1998). HIPASS detects HI masses to a 3σ lower limit of $\sim 10^6 d^2$ M$_\odot$*, corresponding to $\sim 4\times 10^8$ M$_\odot$ at the distance of Fornax.

For this Fornax region survey, 13 HIPASS data cubes were mosaicked together before analysis and trimmed to create a single, large, $\sim 25^\circ \times 25^\circ$ datacube. Mosaicking the cubes improves the effective RMS noise levels at the positions of the HIPASS cube edges and creates a single dataset with relatively smooth coverage across the entire field.

The projected sky area covered by the mosaic is represented in Fig. ??. An image of the data, Fig. ??, shows galaxies in peak flux as bright bands, the length of each being indicative of the velocity width of the detections. In this velocity *vs.* RA map, the cluster galaxies appear to be embedded in a long sheet of galaxies at similar velocities which crosses the mosaic region. The void behind the cluster is clearly seen. The detection at approximately 2900 km s^{-1}, $3^{\rm h}08^{\rm m}$, is at a declination of -23° and is not near the cluster.

3 HI GALAXY DETECTIONS

3.1 Some HIPASS Characteristics

Our survey is limited by two particular selection effects. First we find a clear lower cutoff in peak flux (at $\sim$30 mJy), reflecting the galaxy search technique. Secondly, there is a cutoff in velocity width (at $\sim$50 km s^{-1}) due to the spectral resolution of the survey.

Sources with extended continuum emission can produce standing wave patterns. After bandpass removal a ripple remains in the spectrum, making these sources difficult to parameterize. For example and in particular, we were unable to characterise NGC 1316 (the strong radio source Fornax A) in our data. Spectra of sources within a few arcminutes of the continuum source are also affected by the ripple. In the vicinity of bright continuum sources, the online bandpass removal process distorts the spectral baseline at both the low and high frequency ends, making the detection of nearby HI sources more difficult. The post-processing application of a cleaning algorithm to each cube has improved the bandpass removal and the detection rate close to continuum sources (Barnes et al. 2001).

3.2 Automated Galaxy Finder

After masking the edges of the mosaic, an automated galaxy finding algorithm, MULTIFIND, developed by Kilborn (2001), was used to search for candidate detections.

* for an HI linewidth of 100 km s^{-1}, where d is the distance to the source in Mpc and $H_\circ = 75$ km s^{-1} Mpc $^{-1}$

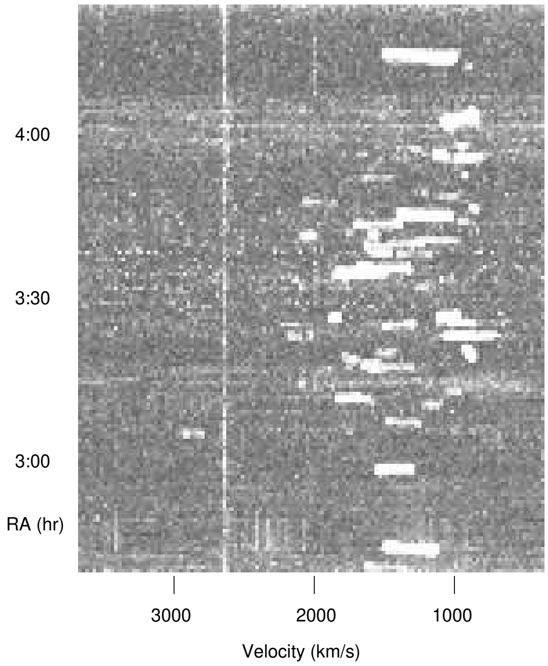

Figure 2. HI flux map from the Fornax mosaic data showing velocities, velocity widths and RA. Detections appear as bright bands in this KVIEW image. The interference band around 2630 km s^{-1} (1408 MHz) is seen as the bright line present through all RA positions. Note that velocities here are heliocentric, without the local group correction (see Section ??).

The galaxy finder searches the data in 3 dimensions, (RA, dec and radial velocity), using MIRIAD routines (Sault, Teuben & Wright 1995) to perform the calculations. In concentrating our search on the Fornax region, the finder was set to search the mosaic in the range 300–3700 km s^{-1} to a lower peak flux limit of 3σ, corresponding on average to about 40 mJy. In MULTIFIND, each pixel is searched in velocity space, plane by plane. Any detections above the preset S/N cutoff and in two or more consecutive velocity planes are retained as possible detections. The search was repeated after each of two rounds of Hanning smoothing in the velocity planes — this type of binning can reduce the RMS noise of the baseline, effectively increasing the S/N, and has the potential to detect extra sources with low S/N profiles. The finder fits a Gaussian to each candidate detection to estimate the central position (although HIPASS sources are not necessarily Gaussian) and uses MBSPECT in MIRIAD to determine spectral parameters.

A final candiate list of over 800 HI detections was generated, with estimates of RA, dec, velocity, velocity width, peak flux and the smoothing level at which the detection was first made.

3.3 Confirmed Detections

The preliminary detection list was first culled by removing the unlikely detections at 2630 $\pm$ 20 km s^{-1} which are known to result from telescope correlator interference (see Fig. 2). To reduce positional redundancies, candidates listed within 2 pixels of each other were grouped together. This left a list of more than 400 to be checked individually. Each candidate detection was visually inspected and parameterized using MIRIAD software packages. An outline of the steps follows:

(i) A moment map of flux integrated over the velocity planes in which the candidate was detected was made.
(ii) A Gaussian was fitted to the moment map and the central positon calculated.
(iii) A spectrum of HI emission at this position was generated and a Guassian-smoothed baseline fitted. Spectral parameters were calculated from unsmoothed spectra: heliocentric recessional velocity (at the midpoint of the 50% and 20% velocity widths), velocity widths (at the 50% and 20% peak flux levels), peak flux and total integrated flux. For the majority of sources, measurements were based on the MIRIAD task MBSPECT using the "point" setting. For extended sources (those so identified in Table 1), the input parameter "sum" was used.

After grouping duplicates, rejecting those unlikely detections which could not be successfully parameterized and those with spectra corrupted by continuum ripple (notably Fornax A and nearby sources), 110 HI detections were confirmed to a maximum velocity cutoff limit of 3700 km s^{-1} . The positions and measured parameters of the detections are listed in Table 1. The spectra are plotted in the Appendix.

The positions of the HI detections relative to the position of the cluster centre are shown in Fig. ??. Plots of the velocity *vs.* RA and dec are shown in Figs. ?? and ?? respectively. There are no detections in front of the cluster and relatively few beyond 2500 km s^{-1} . These plots show clear evidence of void regions. The distribution of galaxies is discussed further in Section ??.

3.4 Optical Counterparts of HI Detections

3.4.1 Optical Identifications

The NASA/IPAC Extragalactic Database (NED†) and the Digitized Sky Survey (DSS‡) were searched for likely optical counterparts within a maximum 15 arcmin radius. Although positional matches were expected to be within ∼3–4 arcmin (Barnes 1998), we searched to larger radii looking for any galaxies which may be associated with the HI detection.

The majority of our detections could be matched to a single optically catalogued counterpart with a published coincident velocity. For 14 objects, a close positional match was found with a single optical galaxy which had no previously published velocity. In at least ∼20% of cases, more than one optical candidate was visible in the DSS images, although in about half of these one of the optical galaxies had a known velocity consistent with the HI object being identified. For 4 galaxies, the published velocity ("$V_{\rm NED}$", column 13, Table 1) is significantly different to our results (columns

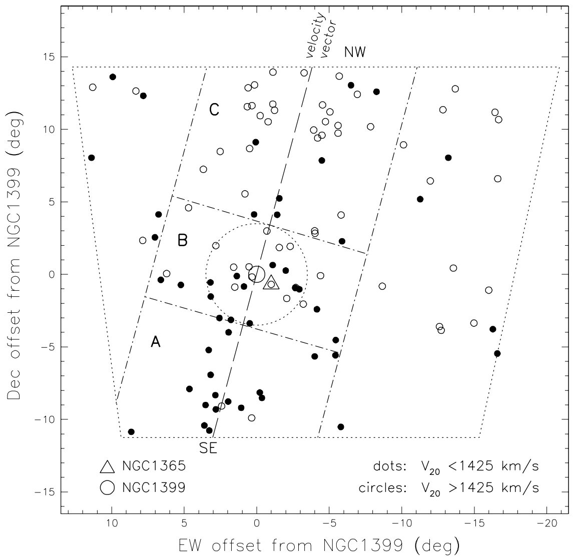

Figure 3. Positions of Fornax Mosaic HIPASS detections. Detections at <1425 km s^{-1} are shown as solid dots, those at >1425 km s^{-1} are shown as open circles. The positions of NGC 1399 (a giant elliptical, not detected) at the cluster centre and NGC 1365 (a large spiral) are shown. The dotted circle indicates the approximate cluster boundary at a radial distance of 3.5° from NGC 1399. A velocity gradient across the structure from SE to NW is suggested, with an approximate angle as indicated by the velocity vector line (long dashes). The detections in the regions A, B & C (dot-dash lines), relative to the vector, are compared in Section ??.

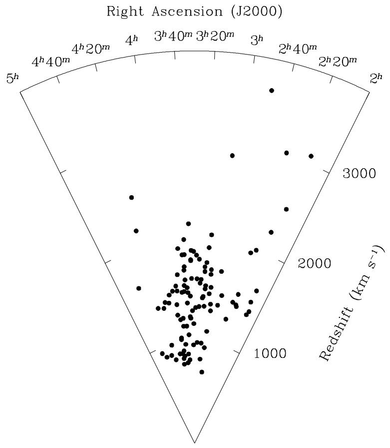

Figure 4. HI detections: Heliocentric velocity vs. RA

† This research has made use of the NASA/IPAC Extragalactic Database (NED) which is operated by the Jet Propulsion Laboratory, California Institute of Technology, under contract with the National Aeronautics and Space Administration. Data used in this paper were current in December, 2001.
‡ The Digitized Sky Survey (DSS), provided by the Space Telescope Science Institute is based on photographic data from the UK Schmidt Telescope.

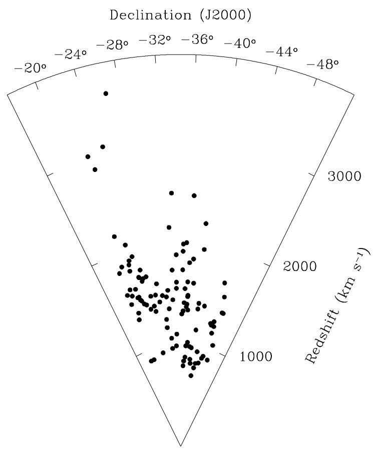

Figure 5. HI detections: Heliocentric velocity vs. declination

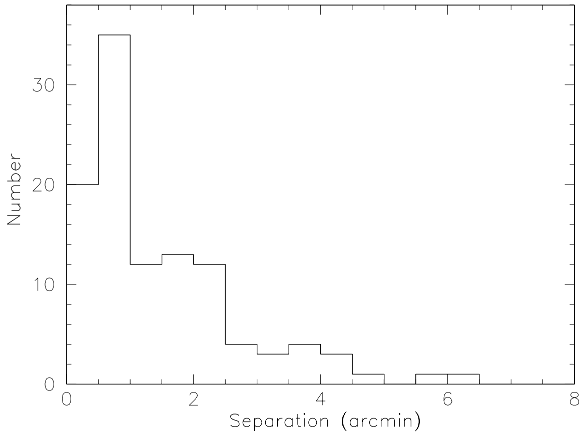

Figure 6. Histogram of positional matches of each HI detection with its most likely optical counterpart. Over 94% of matches are within 4 arcminutes.

4 and 5). A remark in column 16 ("V diff") identifies these detections.

Where the optical match to an HI detection remains uncertain or unknown, it has been marked "C" (for "confused") in column 16 of Table 1. Where a possible optical identification of confused sources is known, it is also noted in column 16. One of our detections, J0317-24, is previously uncatalogued. The optical counterpart of our HI detection J0317−37 is FCCB0035, a galaxy listed as "background" in the Fornax Cluster Catalog . However, we measure a heliocentric velocity of 981 km s^{-1}, indicating that it is more probably a cluster member.

All of these confused or uncertain detections will require follow-up observations at higher resolution to confirm their natures and identities.

A histogram of the projected distance from each detection to its most likely optical counterpart is shown in Fig. ??. The majority of matches are within the expected positional accuracy of 3–4 arcmin, with ∼86% being matched within 3 arcmin and ∼94% matching within 4 arcmin. Our confirmed detections and their likely matches to previously catalogued galaxies are detailed in Table 1.

3.4.2 Morphological Types

Examination of the optical morphologies of our HI detections, as published in NED and as determined from DSS images, revealed that all of our detections were late-type galaxies (or of uncertain morphology). This correlation of morphological type, HI content and proximity to the core of a cluster is discussed further in Section ??.

3.5 Deriving HI Masses and Mass-to-Light Ratios

The HI mass of each detection was calculated using the standard formula (Giovanelli & Haynes 1988), assuming detections to be unresolved in the Parkes telescope beam,

$$M_{HI} = 2.356 \times 10^5\, d^2\, S_{int} \qquad (1)$$

where M_{HI} = HI mass in units of M$_\odot$, d = distance in Mpc and S$_{int}$ = total integrated flux in Jy km s^{-1}, measured from the unsmoothed profiles.

In deriving the HI masses, detections were assumed to be either part of the cluster or in the field. Detections within 3.5° of the cluster centre were all assumed to be at the nominal cluster distance of 20 Mpc. For galaxies more than 3.5° from the cluster centre (i.e. assumed to be field galaxies), the distance was estimated from the Hubble flow. The velocity of each field galaxy was measured from the unsmoothed HI profile at the mid-point of the 20% peak flux level. A Local Group correction was applied, using the IAU convention,

$$V_{LG} = V + 300 \sin l \cos b \qquad (2)$$

where V_{LG} = corrected velocity in km s^{-1}, V = heliocentric velocity in km s^{-1}, l = Galactic longitude and b = Galactic latitude.

Distances to field galaxies were then estimated from the Hubble equation,

$$d = V_{LG}/H_\circ \qquad (3)$$

where d = distance in Mpc. For these calculations, a 'Fornax-consistent' Hubble constant was calibrated such that at the position of the cluster centre, the central cluster galaxy (NGC 1399, l = 236.72°, b = −53.63°, $V_{\rm hel}$ = 1425 km s^{-1}, V_{LG} = 1276 km s^{-1}) has a distance of 20 Mpc in the Hubble equation. The value thus derived and used here is $H_\circ = 64$ km s^{-1} Mpc^{-1}.

The NED database was searched for apparent blue magnitudes of optical counterparts so that, where possible, M_{HI}/L_B values could be estimated for the HI detections. When available, the apparent blue magnitudes m_B, B_T or b_j were recorded and used in calculations of luminosity. The value used and the magnitude type for each detection are indicated in columns 10 and 11 of Table 1.

4 DISCUSSION

4.1 Projected Number Densities of Detections

Greyscale surface number density plots of optical galaxies and positions of HI detections in the same redshift range are illustrated in Fig. **??**. The optical galaxies selected for this comparison include only those in NED with published velocities in the range 500–3700 km s^{-1}. The ellipses refer to optical substructure regions identified by Drinkwater et. al. (2001a), the centre of the optical cluster being at the centre of the larger ellipse. The optical subcluster identified by the smaller ellipse is not distinguished in HI. The HI emission appears to be relatively more extended than the optical cluster region and more structure is suggested by the apparent HI overdensities in regions ∼10° to the north west and south east of the cluster. The south east HI concentration, in particular, has a similar HI content to the Fornax cluster without the optical galaxy overdensity.

The surface number densities of HI detections over the mosaic region are shown in Fig. **??**. Our results suggest that the cluster is detectable as an approximately 3-fold overdensity relative to the field beyond ∼4° from the cluster's optical centre. Within 4° (∼1.4 Mpc), the number density of HI detections is 0.46 ± 0.04 deg^{-2} compared with 0.16 ± 0.03 deg^{-2} in the surrounding field (4° – 10° from the centre). Although the number density of optical galaxies is seen to decline rapidly beyond the nominal cluster boundary, the HI density remains elevated out to radii comparable with the cluster turn-around radius of 2.4 Mpc (∼7°) (Drinkwater et al. 2001a). At these radial distances, galaxies are possibly infalling towards the cluster for the first time and have presumably not yet been stripped of their gas (see Bekki, Couch & Shioya 2002).

Very few HI galaxies are found near the core of the cluster (<1°), and so a statistically significant galaxy density cannot be calculated for this region. In contrast, for galaxies listed in NED with velocities in the range 300–3700 km s^{-1}, number densities are ∼45-fold greater in the core than at 3–4° distant.

HIPASS is biased towards the detection of HI-rich objects. As is evident in Figure 3, the Fornax cluster of galaxies at the centre of the mosaic field is not clearly distinguished in this survey. Of 65 HI detections within a 10° projected radius of the cluster centre, less than 30% are within the nominal optical cluster region (projected radius ∼ 3.5°) — an overdensity of $<2\frac{1}{2}$-fold compared to the number expected for an even distribution. Where the morphology is known, our HI detections are only late-type, a finding which is tightly correlated with the very low HI detection rate close to the cluster core and with the well-established density-morphology relation (Dressler 1980).

Our results clearly indicate that, unlike optical searches, large region HI surveys such as HIPASS will not preferentially detect the core region of galaxy clusters, although a modest overdensity of HI–rich/late-type galaxies may be seen in the cluster infall regions beyond the core.

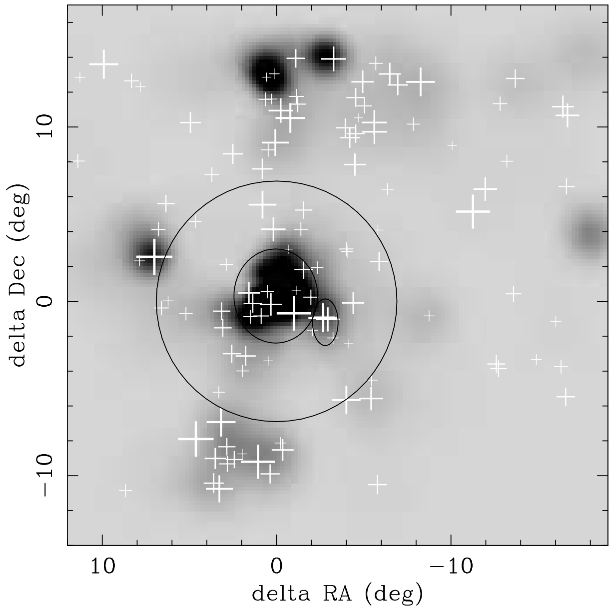

Figure 7. Comparison of the distribution of HI-selected galaxies with optically-selected galaxies in the Fornax region. The grey scale shows an adaptively-smoothed measure of the number density of optically-selected galaxies. The white crosses indicate the positions of all galaxies in the HI sample with the size of the crosses proportional to the logarithm of the integrated HI flux. The two ellipses show the 2σ limits of the main cluster and subcluster and the large circle is at the cluster turn-around radius of ∼7° as defined by the optical sample of Drinkwater et al. (2001a).

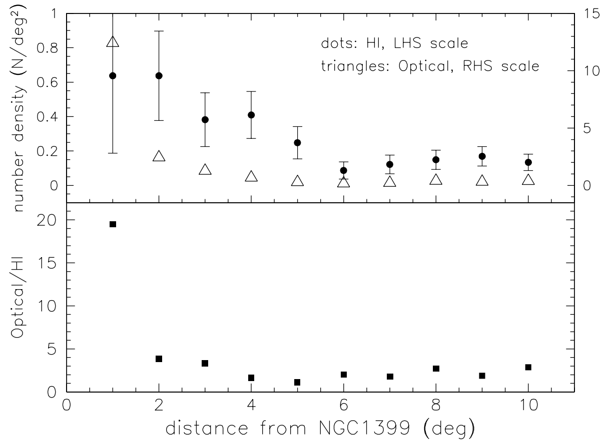

Figure 8. The top panel shows the projected number density of detections at increasing radii from the centre of Fornax. Solid dots and the left hand side (LHS) scale are HI detections, triangles and the RHS scale are for optical counts from NED. Poisson number errors are shown for the HI detections. The lower panel shows the ratio of number densities: Optically catalogued/HI .

4.2 Velocity Measurements and Large Scale Structure

Velocity histograms for ∼200 optical galaxies listed by NED with published redshifts in the Fornax mosaic area and for 110 HI detections in our mosaic are plotted in Fig. **??**. Galaxies within 3.5° of the cluster centre are compared with those field galaxies further than 3.5° from NGC 1399. The cluster is well-defined in velocity, with no objects in front of the cluster and none catalogued between 2200 km s^{-1} and 2800 km s^{-1} in the void behind the cluster. This histogram shows that the large-scale velocity distribution is similar to the cluster velocity distribution. Thus, the large-scale struc-

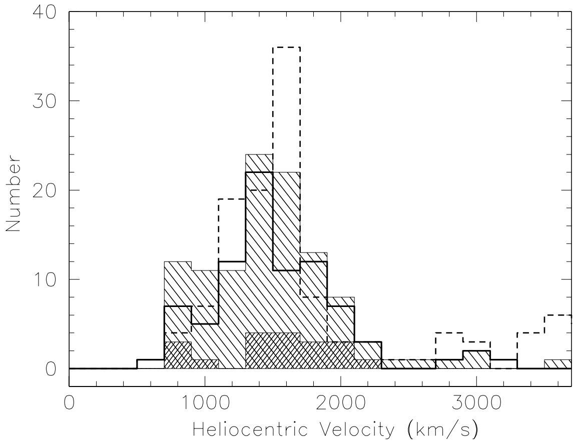

Figure 9. Velocity histograms for Fornax Region galaxies: HI detections within 3.5° of the cluster centre (heavy shading), HI detections beyond 3.5° (light shading), optical cluster galaxies (solid line), optical field galaxies (dashed line). The void in front of and behind the cluster beyond ~2200 km s^{-1} is evident for both HI and optical galaxies.

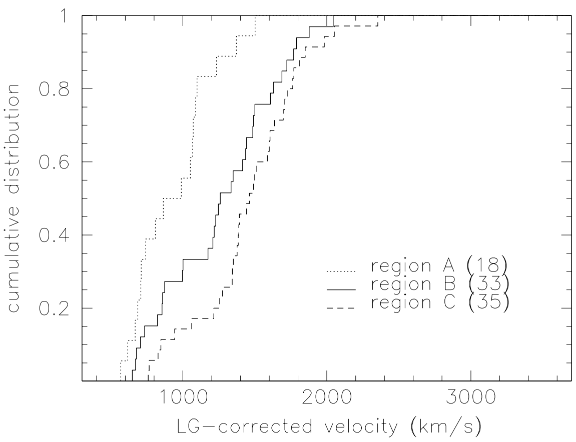

Figure 10. The cumulative distribution function of Fornax Region galaxy velocities. The three curves correspond to the regions A, B and C indicated in Fig. **??** and measure LG-corrected velocities. Galaxy numbers in each region are 18, 33 and 35, respectively.

ture (LSS) is confined to a narrow plane almost perpendicular to the line-of-sight.

The mean heliocentric velocity of the cluster HI galaxies is 1516 ± 95 km s^{-1} , in agreement with the optical results of Drinkwater et al. (2001a). The velocity dispersion (σ_V) of these cluster galaxies is 425 ± 71 km s^{-1} — considerably higher than for the giant cluster galaxies of Drinkwater's optical sample ($\sigma_V = 308 \pm 30$ km s^{-1}) and thus indicative of an infalling population.

In Fig. **??**, the positions of the HI detections relative to the Fornax centre are shown. Large-scale structure is also evident in Fig. **??**, where the galaxies appear to be in a long sheet-like arrangement in which the velocity widths of the galaxies are comparable to the velocity dispersion of the whole sheet.

Our results indicate that there is a measurable velocity gradient, from SE to NW, across the formation. A vector at

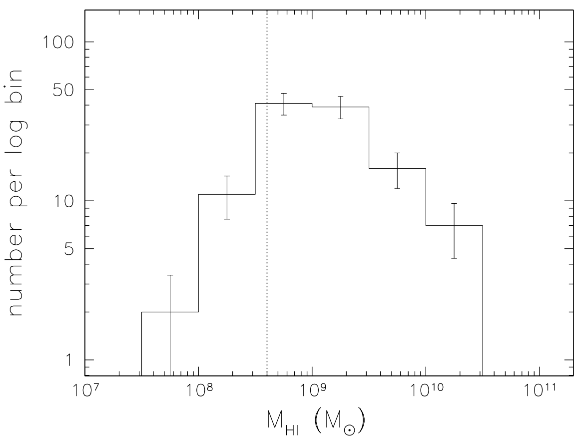

Figure 11. The HI masses of Fornax Region galaxies. Error bars are calculated from number statistics ($\sqrt{N}$). At the Fornax distance, HIPASS detection rates become incomplete below $\sim 4 \times 10^8$ M$_\odot$ (dotted line).

a sky angle of ~75° shows the direction of maximum velocity bias across the region (see Fig. **??**). The cumulative distribution function of the velocity of HI detections is shown in Fig. **??**, comparing the regions A, B and C. The three regions are cut relative to the velocity vector as shown in Fig **??**. Region B extends 3.5° along the vector line and includes all cluster members detected, as well as some non-members outside the 3.5° cluster radius.

After Local Group (LG) correction, the mean velocity of galaxies is 936 ± 63 km s^{-1} in region A, 1266 ± 68 km s^{-1} in region B and 1459 ± 62 km s^{-1} in region C. The KS statistic indicates that the mean LG-corrected velocities of galaxies in regions A and C differ by 523 ± 125 km s^{-1} , significant at the 99.99% confidence level. Comparing the mean peak flux in the two regions, we find it to be lower in region C than in A by up to ~55%, significant at the 95% confidence level. The mean total flux of the two regions is not significantly different. From these comparisons we conclude that a significant gradient in galaxy velocity is measureable across the field.

This gradient closely follows the velocity gradient of optical galaxies evident in Plate 8 of the Nearby Galaxies Atlas, showing the Southern Supercluster in the region of Fornax (Tully & Fisher, 1987).

The radial velocity of the central cD galaxy of the Fornax cluster, NGC 1399, is 1425 km s^{-1}. We have measured the recessional velocity of the three galaxies for which Cepheid distances have been determined in the *Hubble Space Telescope* Key project on the Extragalactic Distance Scale (Kennicutt, Freedman & Mould 1995). Madore et al. (1999) determined the distance to NGC 1365 to be 18.6 ± 0.6 Mpc. We measure a recessional velocity of 1638 km s^{-1} , consistent with the suggestion of Drinkwater et al. (2000a) that the galaxy is in front of NGC 1399 and is falling towards the cluster centre. Prosser et al. (1999) estimated the distance to NGC 1326A to be 18.7 ± 2.0 Mpc. The galaxy is part of the subcluster identified by Drinkwater et al. (2001a) and identified by the small ellipse in Fig **??**. Our measured velocity of 1836 km s^{-1} supports their conclusion that the subcluster is in front of the main cluster and falling inwards. The Cepheid distance to NGC 1425 was calculated to be 22.2 ±

2.7 Mpc (Mould et al. 2000). The large-scale structure we have detected suggests that NGC 1425 may be at a greater distance than the Fornax Cluster proper. From its velocity of 1512 km s^{-1} and location 5.6° North of the cluster, we would expect it to be about 1.5 Mpc more distant than the cluster centre.

4.3 HI Masses and Mass-to-Light Ratios

The HI masses of detections are plotted in Fig. ?? with the highest detection rate being in the $10^{8.5}$–$10^{9.0}$ M$_\odot$ bin, i.e., close to the survey detection limit. For our whole sample, estimated HI mass-to-blue-light ratios (L_B uncorrected for inclination) range from 0.1 to ∼11, with a mean of 1.7, although for a small number of detections the uncertainty in optical identification requires further clarification. The range of HI mass and M_{HI}/L_B values as a function of distance from the centre of Fornax are plotted in Figs. ?? and ??, respectively. The values appear relatively independent of distance to the cluster centre. However, these two plots have ignored possible projection biases. For example, our highest HI mass cluster member is the bright spiral NGC 1365 (J0333-36), circled in Fig. ??. There is evidence that this galaxy is in front of the cluster and falling towards it (Drinkwater et al. 2001a) and therefore its HI mass may be lower than our estimate and its actual distance from the cluster centre greater than the projected distance measured here. This figure indicates that almost 80% of our detections have HI masses below 2×10^9 $M_\odot$ and that most of the higher mass galaxies are outside the cluster region.

The distribution of M_{HI}/L_B values plotted as a function of projected distance to the cluster centre is indicated in Fig. ??. The circled detection, FCC 302, has a low redshift (cz = 803 km s^{-1}), a high M_{HI}/L_B value (∼5.2) and may be behind the cluster and infalling.

The only HI detection seen in projection within the core region is FCC 235 (NGC 1427A), indicated by the triangle in Figs. ?? and ??. Its irregular morphology, particularly high redshift ($cz = 2024$ km s^{-1}) and M_{HI}/L_B value of ∼1.3 support the arguments of Hilker et al. (1997), Chanamé, Infante & Reisenegger (2000) and Drinkwater, Gregg & Colless (2001a) that the galaxy is in front of the cluster centre and infalling. If these data points are ignored, our results are suggestive of reduced M_{HI}/L_B values and HI depletion within 4° of the cluster centre. We measure a cluster mean M_{HI}/L_B value of 1.2 ± 0.3 and a mean of 1.7 ± 0.2 for galaxies more than 4° from the centre, the difference being significant at the ∼90% level. We note here that standard measures of HI deficiency do not include non-detections and interpretation of such results remains thereby inherently uncertain.

The deeper, targeted HI observations of Schröder did, however, detect significantly lower M_{HI}/L_B in Fornax cluster galaxies (0.68 ± 0.15) compared to a selected field sample (1.15 ± 0.10) (Schröder et al. 2001). This is probably explained in part by their more sensitive observations and larger sample of cluster galaxies. In addition, Schröder et al. also found that the cluster galaxies show significant HI depletion as measured by the Solanes parameter (Solanes, Giovanelli & Haynes 1996). Although HI depletion measurements were beyond the scope of our observations, our HI measurements are consistent with Schröder's results for the 23 common galaxies observed.

In Fig. ??, the distribution of M_{HI}/L_B and M_{HI} values is plotted. Of detections with $M_{HI}/L_B > 1$, ∼80% are fairly low M_{HI} galaxies with $M_{HI} < 2 \times 10^9$ M$_\odot$. These galaxies are also all of low luminosity. Although corrections for inclination have not been made here, we conclude that most of the high M_{HI}/L_B detections are small or dwarf galaxies. Again, projection effects have not been considered in this plot.

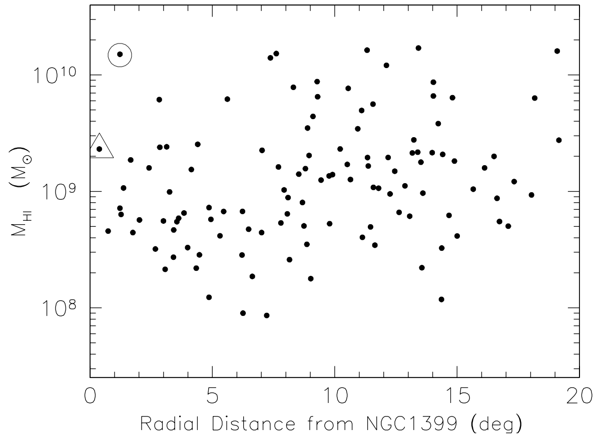

Figure 12. More than 50% of detections have an HI mass less than 10^9 M$_\odot$. Most of the high HI mass detections are outside the cluster region. The circled point, NGC 1365, and NGC1427A, identified by the triangle, are discussed further in Section ??.

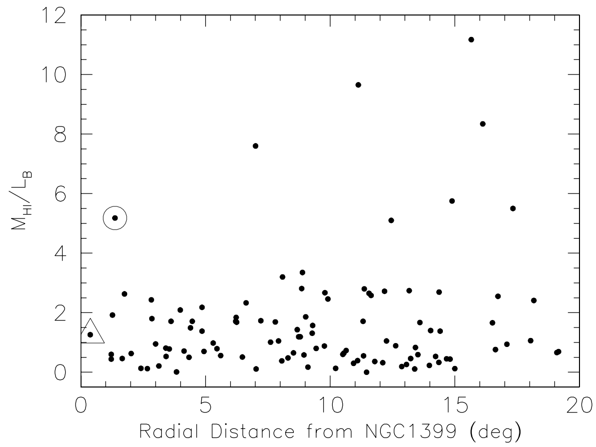

Figure 13. The M_{HI}/L_B ratios of detections, as a function of projected distance from the cluster centre, are fairly evenly distributed across the mosaic region. Almost 50% have a M_{HI}/L_B ratio >1 M$_\odot$/L$_\odot$. The circled detection is J0345-35 (FCC302) which has a high M_{HI}/L_B (5.2) and a low redshift (cz = 803 km s^{-1}). The measured radial offset may thus be biased by a projection effect. The galaxy may be beyond the cluster and infalling. The object J0340-35 (FCC235) (identified by the triangle) has a very high redshift of 2028 km s^{-1} and is probably in front of the cluster centre and infalling.

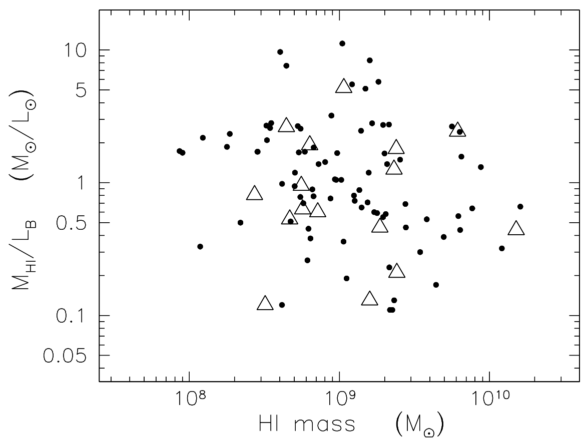

Figure 14. In this plot of M_{HI} *vs.* M_{HI}/L_B , cluster detections are shown as triangles and detections outside the cluster are shown as solid dots. The majority of detections (∼84%) with M_{HI}/L_B >1 are small or dwarf galaxies with low luminosity and low HI masses ($< 2 \times 10^9$ $M_\odot$).

5 CONCLUSIONS

We have mosaicked an area of ∼620 square degrees around the Fornax cluster of galaxies using standard HIPASS cubes. An intensive search of this cube has resulted in a catalogue of 110 galaxies. Of these, 14 galaxies have newly determined redshifts, 4 have velocity measurements significantly different to values published for the likely optical counterpart and for about 10% the optical identification is currently uncertain. This HI catalogue can be used in studies of the large-scale structure around the Fornax cluster, the morphological evolution of galaxies and the morphology-density relation in the cluster and field environments.

Our main results are:

(i) A strong indication that cluster centres which are readily apparent in the counts of optical galaxies are only detected as HI overdensities of a few times the density of HI-detected galaxies in the field.

(ii) The region of overdensity of HI galaxies extends for several degrees (∼1.7 Mpc) around the cluster, including the cluster infall region.

(iii) The large-scale HI structure around the Fornax cluster is confined to a plane with similar velocity width to velocity dispersion we measure for the cluster itself (425 ± 71 $\mathrm{km\,s^{-1}}$). This plane is almost perpendicular to the line-of-sight but we measure a significant difference of ∼500 $\mathrm{km\,s^{-1}}$ in the redshifts of galaxies in the NW region compared to the SE region. Further analysis of the LSS will enable peculiar velocities to be decoupled from the general cosmological expansion.

Published optical magnitudes have been used to estimate M_{HI}/L_B ratios. From this we can conclude that:

(i) There is no unambiguous signal of HI depletion in the small number of HI-detected galaxies near the cluster core.

(ii) Only a small fraction of galaxies are detected in HI near the cluster core. Morphologically, the HI -detected galaxies are all late-type and these are less likely to be found in regions of high galactic density.

(iii) The galaxies with higher M_{HI}/L_B are all dwarf-type galaxies.

Further work intended in these studies includes the resolution of "confused" sources by deeper HI imaging at the ATCA (Australia Telescope Compact Array).

Many questions about galaxy evolutionary processes in and around clusters remain unanswered. Our studies indicate that the core of the Fornax cluster is deficient in HI-rich galaxies, a finding which is tightly correlated with the morphologies of galaxies in the core. However, the evolution of galaxies in the cluster environment is currently poorly understood and future work will be aimed at further elucidation of these processes.

NOTES FOR TABLE 1.

Explanatory notes for the columns in Table 1:
(**Note:** All values are from unsmoothed spectra.)
Col. (1) HIPASS name (Jhhmm-dd). Suffixes a, b, etc. are used to name uniquely HIPASS detections when required.
Cols. (2) & **(3)** HI detection center position in R.A. and dec. (J2000).
Cols. (4) & **(5)** HI Heliocentric systemic radial velocity in $\mathrm{km\,s^{-1}}$ (optical convention) at the midpoint of the 50% width (V_{50}) and 20% width (V_{20}), respectively, measured from unsmoothed spectra.
Cols. (6) & **(7)** 50% & 20% HI velocity widths in $\mathrm{km\,s^{-1}}$ (W_{50} & W_{20}).
Col. (8) HI peak flux in Jy.
Col. (9) Total integrated HI flux density in $\mathrm{Jy\,km\,s^{-1}}$.
Col. (10) Apparent blue magnitude (from NED, measurement type shown in Col. (11).
Col. (11) Type of magnitude measurement in Col. (10).
Col. (12) HI mass-to-blue light ratio (M_{HI}/L_B).
Col. (13) Optical galaxy velocity ($\mathrm{km\,s^{-1}}$) recorded in NED.
Col. (14) Projected separation in arcminutes (d′) of the positions of the HI detection and the likely corresponding optical galaxy.
Col. (15) Name(s) of the likely matching optical galaxy.
Col. (16) Remarks — including the names(s) of possible optical galaxy match(es) where the match is uncertain. These detections are labelled "C" ("confused"). Derived values shown in the table proper refer to the galaxy named in Col. (14). For detections labelled "V diff", the HI velocity differs significantly from the published optical value(s). The comment "new V" indicates that a velocity measurement has not previously been published.

6 ACKNOWLEDGEMENTS

M.W. gratefully acknowledges the support of the University of Melbourne in the provision of a Melbourne Research Scholarship. We are most appreciative of the anonymous referee's helpful comments which have resulted in valuable improvements to this work.

REFERENCES

Andreani P., Casoli F., Gerin M., 1995, A&A, 300, 43
Barnes D.G., 1998, PhD Thesis, University of Melbourne
Barnes D.G., Staveley-Smith L., Webster R.L., Walsh W., 1997, MNRAS, 288, 307
Barnes D.G., Staveley-Smith L., de Blok W.J.G. et al. 2001, MNRAS, 322, 486
Bekki K., Couch W.J., Shioya Y., 2002, ApJ accepted, (astro-ph/0206207)
Bureau M., Mould J.R., Staveley-Smith, L., 1996, ApJ, 463, 60
Chanamé J., Infante L., Reisenegger A., 2000, ApJ, 530, 96
de Vaucouleurs G., de Vaucouleurs A., Corwin Jr. H.G., Buta R.J, Paturel G., Fouque P., 1991, Third Reference Catalogue of Bright Galaxies, Vols. I–III (Springer, New York) (RC3)
Dressler A., 1980, ApJ, 236, 351
Drinkwater M.J., Gregg M.D., 1998, MNRAS, 296, 15
Drinkwater M.J., Phillipps S., Jones J.B., Gregg M.D., Deady J.H., Davies J.I., Parker Q.A., Sadler E.M., Smith R.M., 2000, A&A, 355, 900
Drinkwater M.J., Gregg M.D., Colless M., 2001a, ApJ, 548, 139
Drinkwater M.J., Gregg M.D., Holman B.A., Brown M.J.I., 2001b, MNRAS, 326, 1076
Ferguson H.C., 1989a, Ap&SS, 157, 227
Ferguson H.C. 1989b, AJ, 98, 367
Giovanelli R., Haynes M.P., 1988, in Verschuur G., Kellermann K. eds, "Galactic and Extragalactic Radio Astronomy", 2nd edn. Springer-Verlag, New York, 525
Hilker M., Bomans D.J., Infante L., Kissler-Patig M., 1997, A&A, 327, 562
Kennicutt Jr. R.C., Freedman W.L., Mould J.R., 1995, AJ, 110, 1476
Kilborn V.A., 2001, PhD Thesis, University of Melbourne
Madore B.F., Freedman W.L., Silbermann N., et al., 1999, ApJ, 515, 29
Mould J.R., Hughes S. M. G., Stetson P.B., et al., 2000, ApJ, 528, 655
Prosser C.F., Kennicutt Jr. R.C., Bresolin F., et al., 1999, ApJ, 525, 80
Sault R.J., Teuben P.J., Wright M.C.H., 1995, in Shaw R.A., Payne H.E., Hayes J.J.E., eds, ASP Conference Series Vol. 77, Astronomical Data Analysis Software and Systems IV, 433.
Schröder A., Drinkwater M.J., Richter O.-G., 2001, A&A, 376, 98
Solanes J.M., Giovanelli R., Haynes M.H., 1996, ApJ, 461, 609
Staveley-Smith L., Wilson W.E., Bird T.S., Disney M.J., et al., 1996, PASA, 13, 243
Tully R.B., Fisher J.R., 1987, Atlas of Nearby Galaxies , C.U.P., Cambridge

APPENDIX A: HI SPECTRA

The HI spectra of all detections are plotted in the Appendix. The profiles show heliocentric radial velocity (optical convention) in km s^{-1} *vs.* flux in Jy. Spectra shown here have been Hanning smoothed and a Gaussian-smoothed baseline fitted over the velocity range shown. Several spectra have been masked before flux measurements were made — the detection being measured is indicated with an arrow and the regions masked are enclosed in dotted lines (see *Notes* below). Dashed lines on the spectra show the velocity range within which V_{50} and V_{20} were determined, with the pairs of dots on the spectra delineating the velocity widths, W_{50} and W_{20}, at 50% and 20% of the peak flux. Flux and velocity width measurements were made on unsmoothed spectra and so may vary slightly from values suggested by the smoothed spectra.

APPENDIX B: NOTES ON SELECTED SPECTRA

J0308-23 The HI emission at ∼2880 km s^{-1} is from IC1892. The extra emission suggested at a slightly higher velocity but below the 3σ limits, is possibly from MCG-04-08-029 with a NED velocity of 3016 km s^{-1}.

J0322-37 Nearby emission at ∼1200–1350 km s^{-1} has been masked before fitting the baseline to this spectrum.

J0323-36 The central (arrowed) emission in this spectrum is from NGC1326. Emissions from the nearby interacting galaxies J0325-36a (NGC1326A, 1836 km s^{-1}) and J0325-36b (NGC1326B, 1006 km s^{-1}) are also seen in this spectrum but have been masked out in measurements.

J0325-36a Emission from J0325-36b (NGC1326B) is also seen in this spectrum.

J0325-36b Emission from J0325-36a (NGC1326A) is also seen in this spectrum.

J0335-32 This detection is at the lowest peak flux of the observations described in this work. We have listed it as "confused" since the spectrum shows considerable baseline ripple, the positional discrepancy with the optical coordinates is greater (4.8 arcmin) than for most confirmed detections and our velocity measurement differs significantly from published optical values (see, for example, de Vaucouleurs et al., 1991).

J0341-22 Considerable ripple can be seen in this spectrum and if the fitted baseline shown is subtracted, the profile more obviously has the typical double-horned shape of an inclined spiral galaxy (NGC1415). The velocity and velocity width measurements are in close agreement with the values published by Andreani, Casoli & Gerin (1995).

J0359-45 The main emission in this spectrum is from the irregular galaxy known as the Horologium Dwarf. Also seen at a slightly higher velocity is emission from the nearby edge on spiral ESO249-G035 which has a published (NED) velocity of 1031 km s^{-1} but is below the flux cutoff levels of this survey.

This paper has been produced using the Royal Astronomical Society/Blackwell Science LaTeX style file.

Table 1: Properties of Fornax Region Detections

(1) *HIPASS NAME*	(2) *RA* (J2000)	(3) *Dec* (J2000)	(4) V_{50} km/s	(5) V_{20} km/s	(6) W_{50} km/s	(7) W_{20} km/s	(8) S_{pk} Jy	(9) S_{int} Jy km/s	(10) *app. magn*	(11) *magn type*	(12) M/L	(13) $V_{\rm NED}$ km/s	(14) d'	(15) *other name(s)/ likely opt. ID*	(16) *remarks*
J0210-40	02:10:41.6	−40:54:24	1416	1423	159	191	0.075	9.36	14.28	m_B	1.1	1415	0.9	ESO298-G015	
J0214-39	02:14:25.9	−39:13:39	1377	1374	77	94	0.078	5.42	14.74	B_T	0.9	3991	2.5	ESO298-G023	V diff
J0218-36	02:18:49.7	−36:32:26	2498	2498	208	219	0.046	4.80	17.24	B_T	8.3	2456	2.1	ESO355-G005	
J0221-38	02:21:36.5	−38:48:54	2231	2233	58	76	0.081	4.02	17.75	B_T	11.2	...	1.7	ESO298-G033	new V
J0222-28	02:22:33.5	−28:51:38	1635	1656	129	186	0.079	8.40	16.18	B_T	5.5	...	1.0	ESO415-G023	new V
J0224-24	02:24:59.2	−24:47:03	3080	3077	188	257	0.188	30.57	12.48	m_B	0.7	3092	1.3	NGC0922	
J0226-24	02:26:24.1	−24:16:39	1510	1512	192	221	0.131	22.57	12.86	m_B	0.7	1515	1.0	UGCA032	
J0232-35	02:32:14.7	−35:01:18	2014	2035	202	261	0.059	8.28	13.77	m_B	0.6	2020	0.8	ESO355-G026	
J0232-39	02:32:42.5	−39:18:41	1435	1433	114	135	0.092	9.67	14.73	m_B	1.7	1399	0.9	NGC0986A	
J0233-39	02:33:34.5	−39:02:54	1973	1974	91	121	0.143	10.93	11.67	m_B	0.1	2005	0.3	NGC0986	
J0238-27	02:38:57.4	−27:24:32	1420	1407	48	104	0.082	4.07	12.85	m_B	0.1	1375	2.5	IC1826	
J0239-22	02:39:07.9	−22:39:41	3027	3026	237	256	0.100	12.52	14.85	m_B	2.4	3027	0.1	ESO479-G020	
J0242-24	02:42:13.1	−24:06:13	1541	1570	149	238	0.053	6.72	14.28	B_T	0.8	1431	2.2	ESO479-G025	
J0243-29	02:43:44.6	−29:00:33	1452	1451	313	331	0.144	25.90	12.27	m_B	0.5	1447	0.4	NGC1079	
J0246-30	02:46:17.6	−30:16:19	1271	1271	371	405	0.776	151.60	9.96	m_B	0.3	1275	0.3	NGC1097	
J0253-26	02:53:14.0	−26:31:12	3589	3589	40	55	0.082	3.03	16.53	B_T	2.7	...	0.0	ESO480-G010	new V
J0255-36	02:55:31.8	−36:16:21	1492	1484	166	229	0.038	4.73	15.14	B_T	1.2	1438	4.2	ESO356-G018	
J0302-22	03:02:38.1	−22:51:46	1390	1388	270	289	0.343	64.70	11.23	m_B	0.4	1396	0.3	NGC1187	
J0303-25	03:03:46.9	−25:16:07	1728	1717	114	148	0.040	4.33	14.92	m_B	0.9	1726	0.8	UGCA050	
J0305-45	03:05:06.6	−45:58:31	1391	1375	187	231	0.077	11.15	14.07	m_B	1.0	1391	0.8	ESO248-G002	
J0308-23	03:08:19.7	−23:02:21	2883	2879	173	198	0.112	14.69	13.77	m_B	1.0	2888	2.1	IC1892-Pr	C, pair & MCG-04-08-029
J0309-41	03:09:42.7	−41:01:36	955	957	129	150	0.256	27.16	13.11	m_B	1.0	951	0.9	ESO300-G014	
J0310-39	03:10:02.4	−39:58:54	711	708	30	45	0.155	4.69	15.56	B_T	1.7	...	2.0	ESO300-G016	new V
J0310-22	03:10:22.1	−22:24:31	1325	1324	250	272	0.143	23.49	13.56	m_B	1.4	1328	0.5	IC1898	
J0310-33	03:10:23.2	−33:10:04	1118	1117	116	151	0.119	11.80	14.62	m_B	1.8	1121	0.7	ESO357-G007	
J0311-31	03:11:12.6	−31:21:35	1558	1564	38	61	0.093	3.67	17.43	b_j	7.6	1625	3.8	2dFGRSS470Z147	
J0313-25a	03:13:34.6	−25:43:31	1686	1684	235	252	0.171	34.26	11.78	m_B	0.4	1697	0.6	NGC1255	
J0313-25b	03:13:42.0	−25:11:34	1733	1732	170	185	0.260	36.51	13.79	m_B	2.6	1738	0.5	UGCA061	
J0313-21	03:13:58.3	−21:47:41	1493	1499	122	150	0.074	5.41	13.95	m_B	0.4	1507	2.1	NGC1258	
J0316-24	03:16:21.3	−24:14:59	2078	2056	56	127	0.137	8.84	15.36	m_B	2.7	2087	4.0	UGCA063	
J0316-35	03:16:51.6	−35:32:29	1570	1570	128	148	0.221	21.37	13.75	m_B	1.5	1567	0.3	ESO357-G012(FCC003)	
J0317-41	03:17:13.8	−41:06:36	838	839	38	75	1.775	82.87	9.44	m_B	0.1	839	0.9	NGC1291	extended
J0317-37	03:17:26.3	−37:51:52	997	992	44	70	0.060	2.96	16.31	b_j	2.2	...	1.5	FCCB0035	new V, cluster member
J0317-24	03:17:34.9	−24:55:05	1949	1961	51	83	0.053	2.48	...	...	...	...	...	...	previously uncatalogued
J0318-27	03:18:13.2	−27:36:09	1365	1365	237	251	0.135	22.40	12.68	m_B	0.6	1367	0.6	NGC1292	
J0318-25	03:18:29.0	−25:51:28	1800	1785	205	253	0.076	10.47	13.54	m_B	0.6	1802	1.7	UGCA064	
J0318-23	03:18:38.7	−23:45:56	1538	1531	81	114	0.161	12.58	15.66	m_B	5.1	1535	1.4	UGCA065	
J0319-32a	03:19:23.6	−32:37:23	1756	1757	61	80	0.090	4.75	15.30	av	1.4	1673	1.6	LSBGF418-059(FCC009)	
J0319-32b	03:19:33.1	−32:26:54	1461	1438	132	190	0.062	5.81	14.34	m_B	0.7	1451	1.0	IC1913(FCC010)	
J0319-26	03:19:47.0	−26:02:53	1710	1710	96	115	0.214	15.62	11.40	m_B	0.1	1703	1.2	NGC1302	
J0321-25	03:21:03.6	−25:29:44	1447	1454	133	169	0.108	12.05	13.60	m_B	0.7	1469	1.0	NGC1306	
J0322-37	03:22:19.2	−37:30:07	1629	1630	71	87	0.091	5.13	...	...	...	1624	5.9	SGC0320.1-3747	
J0323-36	03:23:52.8	−36:29:02	1359	1359	240	257	0.175	25.62	11.42	m_B	0.2	1360	1.4	NGC1326(FCC029)	
J0324-21	03:24:25.1	−21:33:36	1592	1592	329	356	0.164	29.53	12.28	m_B	0.5	1589	1.0	NGC1325	
J0325-36a	03:25:08.4	−36:21:39	1830	1831	75	89	0.382	25.37	13.77	m_B	1.8	1836	0.1	NGC1326A(FCC037)	C, interacting with NGC1326B
J0325-36b	03:25:17.5	−36:23:31	1002	999	160	180	0.447	65.10	13.07	m_B	2.4	1006	0.7	NGC1326B(FCC039)	C, interacting with NGC1326A
J0327-33	03:27:22.9	−33:30:57	1635	1635	180	218	0.052	5.92	14.65	m_B	1.0	1624	2.3	ESO358-G005(FCC053)	
J0328-37	03:28:05.9	−37:06:32	1869	1867	60	73	0.071	3.39	12.97	m_B	0.1	1859	2.8	NGC1341(FCC062)	
J0328-35	03:28:40.6	−35:11:42	1349	1349	199	214	0.055	6.03	14.18	m_B	0.6	1360	1.9	NGC1351A(FCC067)	
J0330-33	03:30:59.6	−33:36:15	1907	1934	390	459	0.088	16.88	11.39	m_B	0.1	1905	2.3	NGC1350(FCC088)	
J0331-30	03:31:16.5	−30:12:30	1189	1202	129	177	0.080	10.11	13.87	m_B	0.8	1195	3.0	ESO418-G008	
J0331-31	03:31:53.2	−31:20:19	978	964	133	172	0.048	5.48	14.04	m_B	0.5	972	0.5	ESO418-G009	
J0333-24	03:33:06.5	−24:08:33	1917	1918	166	180	0.078	8.76	15.40	m_B	2.8	1915	1.1	ESO482-G005	
J0333-34	03:33:06.8	−34:48:27	1318	1343	187	249	0.057	6.73	15.28	m_B	1.9	1388	0.0	ESO358-G015(FCC113)	
J0333-36	03:33:33.3	−36:08:27	1638	1638	370	399	0.662	159.80	10.23	m_B	0.4	1636	0.6	NGC1365(FCC121)	
J0333-23	03:33:37.7	−23:42:38	1815	1824	228	258	0.039	6.28	13.55	m_B	0.4	1812	2.5	IC1952	
J0333-21a	03:33:40.9	−21:30:21	1824	1860	124	212	0.108	12.07	12.35	m_B	0.2	1867	1.6	IC1953	

Table 1: Properties of Fornax Region Detections

(1) *HIPASS NAME*	(2) *RA* (J2000)	(3) *Dec* (J2000)	(4) V_{50} km/s	(5) V_{20} km/s	(6) W_{50} km/s	(7) W_{20} km/s	(8) S_{pk} Jy	(9) S_{int} Jy km/s	(10) *app. magn*	(11) *magn type*	(12) M/L	(13) $V_{\rm NED}$ km/s	(14) d'	(15) *other name(s)/ likely opt. ID*	(16) *remarks*
J0335-24	03:35:00.5	−24:55:53	1463	1462	387	403	0.373	73.23	11.49	m_B	0.6	1471	0.3	NGC1367(NGC1371)	
J0335-32	03:35:10.3	−32:27:27	2182	2184	86	99	0.036	2.27	13.87	m_B	0.2	1459	4.8	ESO358-G025(FCC152)	C, marginal detection, V diff
J0336-43	03:36:30.1	−43:58:11	1243	1244	278	295	0.110	21.22	12.85	m_B	0.7	1243	0.8	IC1970	
J0337-43	03:37:20.5	−43:36:05	1259	1252	37	84	0.087	3.85	18.11	b_j	14.9	...	1.6	LSBGF249-015	C, & ESO249-IG008
J0337-24	03:37:26.5	−24:30:37	1498	1503	178	208	0.192	31.03	11.62	m_B	0.3	1493	0.7	NGC1385	
J0338-26	03:38:49.2	−26:20:39	1396	1396	450	469	0.179	47.01	10.51	m_B	0.2	1407	0.7	NGC1398	
J0339-22	03:39:07.8	−22:23:39	1878	1875	37	57	0.099	3.41	13.83	m_B	0.3	4293	0.8	NGC1403	V diff
J0339-31	03:39:19.9	−31:18:57	1080	1068	306	353	0.133	30.88	12.54	m_B	0.7	1075	0.7	NGC1406	
J0339-23	03:39:55.0	−23:49:02	1626	1631	84	123	0.046	2.60	16.63	B_T	2.6	...	3.5	ESO482-G027	new V
J0340-35	03:40:07.5	−35:37:51	2028	2026	86	120	0.282	24.51	13.42	m_B	1.3	2028	0.6	NGC1427A(FCC235)	
J0340-45	03:40:30.3	−45:21:07	1548	1548	86	106	0.154	12.89	14.84	B_T	2.5	1274	0.9	IC1986	V diff
J0340-26	03:40:41.1	−26:47:04	1723	1734	78	119	0.072	5.38	15.20	m_B	1.4	1765	0.1	ESO482-G032	
J0340-38	03:40:58.1	−38:49:37	831	827	55	73	0.054	2.88	15.26	b_j	0.8	816	1.7	Wombat1	(Barnes et al. 1997)
J0341-22	03:41:01.7	−22:35:17	1571	1570	350	360	0.053	9.09	12.42	m_B	0.2	1585	1.9	NGC1415	
J0341-34	03:41:05.6	−34:56:02	1757	1752	165	193	0.051	4.84	13.92	m_B	0.4	1734	1.3	ESO358-G051(FCC263)	C, & FCC256
J0341-23	03:41:18.9	−23:53:18	1877	1852	195	253	0.045	6.23	13.67	m_B	0.4	1890	3.3	ESO482-G035	C, & LSBGF482-018
J0342-29	03:42:12.6	−29:53:55	1511	1512	354	374	0.312	56.77	11.62	m_B	0.6	1512	0.4	NGC1425	
J0342-36	03:42:51.7	−36:17:26	889	890	82	99	0.105	7.61	13.89	m_B	0.6	895	2.4	NGC1437A(FCC285)	
J0344-44	03:44:30.1	−44:39:16	1167	1170	392	415	0.577	154.63	11.46	m_B	1.3	1164	0.6	NGC1448	
J0345-35	03:45:12.5	−35:34:07	803	804	72	100	0.156	11.34	15.79	m_B	5.2	803	0.2	ESO358-G060(FCC302)	
J0345-36	03:45:58.8	−36:19:54	1505	1531	143	217	0.039	4.71	16.01	B_T	2.6	1497	1.7	NGC1437B(FCC308)	
J0346-34	03:46:15.4	−34:57:26	1942	1928	266	315	0.101	19.74	12.57	m_B	0.5	1932	1.1	ESO358-G063(FCC312)	
J0347-38	03:47:34.4	−38:35:18	987	997	151	192	0.110	14.73	14.30	m_B	1.7	987	0.6	ESO302-G009(FCC322)	
J0348-39	03:48:33.3	−39:27:05	1168	1169	29	46	0.157	4.93	15.49	B_T	1.7	...	1.7	ESO302-G?010	new V
J0349-44	03:49:29.3	−44:13:00	1247	1250	53	66	0.054	2.69	16.24	B_T	1.9	...	2.1	ESO249-G021	new V
J0349-26	03:49:47.0	−26:59:06	1523	1519	212	237	0.101	14.13	13.95	m_B	1.2	1525	1.2	UGCA085	
J0351-38	03:51:37.8	−38:27:33	872	873	65	85	0.183	11.47	14.79	m_B	2.1	881	0.7	ESO302-G014	
J0352-33	03:52:00.8	−33:28:02	1573	1587	129	173	0.050	4.95	14.21	m_B	0.4	1574	0.0	ESO359-G003(FCC338)	
J0352-44	03:52:04.5	−44:31:34	1684	1688	133	152	0.085	9.58	13.95	m_B	0.8	1720	0.8	NGC1476	
J0354-36a	03:54:14.8	−36:00:44	1389	1385	226	250	0.077	10.50	15.82	B_T	4.9	1399	3.8	ESO359-G005	C, & IC2006
J0354-43	03:54:15.6	−43:46:48	924	931	86	140	0.123	10.86	15.17	m_B	2.8	1078	1.4	ESO249-G026	
J0354-36b	03:54:20.3	−36:59:03	1038	1044	168	195	0.095	12.33	13.65	m_B	0.8	1040	0.9	NGC1484	
J0354-44	03:54:23.0	−44:45:54	1236	1236	103	121	0.096	8.30	15.41	m_B	2.7	1272	1.3	ESO249-G027	
J0355-28	03:55:12.5	−28:12:45	1527	1522	154	188	0.051	5.83	13.68	m_B	0.4	1555	4.0	IC2007	
J0355-42	03:55:43.7	−42:22:50	848	843	203	229	0.421	63.89	12.30	m_B	1.2	848	0.9	NGC1487-GPr	C, merger
J0355-40	03:55:56.3	−40:40:28	792	791	84	96	0.060	4.12	15.67	B_T	1.7	...	0.9	ESO302-G021	new V
J0357-46	03:57:25.2	−46:13:15	1054	1053	107	126	0.470	45.47	11.85	m_B	0.6	1054	0.8	NGC1493	
J0358-44	03:58:15.3	−44:27:51	1284	1280	211	235	0.109	19.70	13.26	m_B	0.9	1279	1.0	NGC1495	
J0359-45	03:59:12.8	−45:52:24	898	898	67	84	0.229	13.95	16.24	m_B	9.7	901	0.5	HorologiumDwarf	
J0400-30	04:00:23.2	−30:51:34	1494	1486	64	150	0.062	4.61	14.24	m_B	0.5	1505	4.3	ESO419-G013	
J0403-43	04:03:59.7	−43:20:45	900	903	240	272	1.149	220.57	11.27	m_B	1.3	896	1.0	NGC1512	extended
J0404-36	04:04:25.6	−36:10:47	1416	1415	126	138	0.048	4.65	14.95	m_B	1.0	1406	0.0	ESO359-G016	
J0408-35	04:08:59.2	−35:24:16	1430	1429	80	98	0.050	3.12	15.99	B_T	1.7	...	2.9	ESO359-G022	new V
J0410-31	04:10:11.3	−31:19:12	1374	1358	97	148	0.065	6.49	15.18	m_B	1.7	1387	4.3	UGCA089	
J0411-35	04:11:04.8	−35:49:55	850	848	68	87	0.106	7.09	15.43	B_T	2.3	...	1.5	ESO359-G024	new V
J0411-32	04:11:54.8	−32:53:46	1001	1200	105	539	0.925	227.90	11.16	m_B	1.3	1196	2.5	NGC1532/1531-GPr	C, pair, extended
J0412-23	04:12:31.2	−23:08:15	902	892	66	99	0.054	3.60	14.06	m_B	0.3	823	2.7	ESO483-G013	
J0414-22	04:14:39.2	−22:48:30	2189	2198	150	176	0.067	7.45	16.36	b_J	5.8	...	0.3	APMBGC483-129-114	new V
J0415-33	04:16:00.0	−33:06:25	2522	2519	95	111	0.051	2.78	16.79	B_T	3.2	2616	3.4	ESO360-G003	
J0421-21	04:21:16.5	−21:50:24	898	898	176	192	0.446	60.18	12.74	m_B	1.7	906	0.8	UGCA090(ESO550-G024)	
J0427-22	04:27:28.0	−22:33:17	1637	1644	118	207	0.046	4.26	16.08	B_T	2.5	...	1.9	ESO484-G019	new V
J0428-46	04:28:35.9	−46:18:32	1388	1397	57	92	0.068	4.00	16.21	B_T	2.7	...	1.2	ESO251-G003	new V
J0429-27	04:29:48.5	−27:24:23	947	945	69	99	0.093	6.28	14.45	m_B	0.8	906	1.7	NGC1592-GGptri	C, group triple

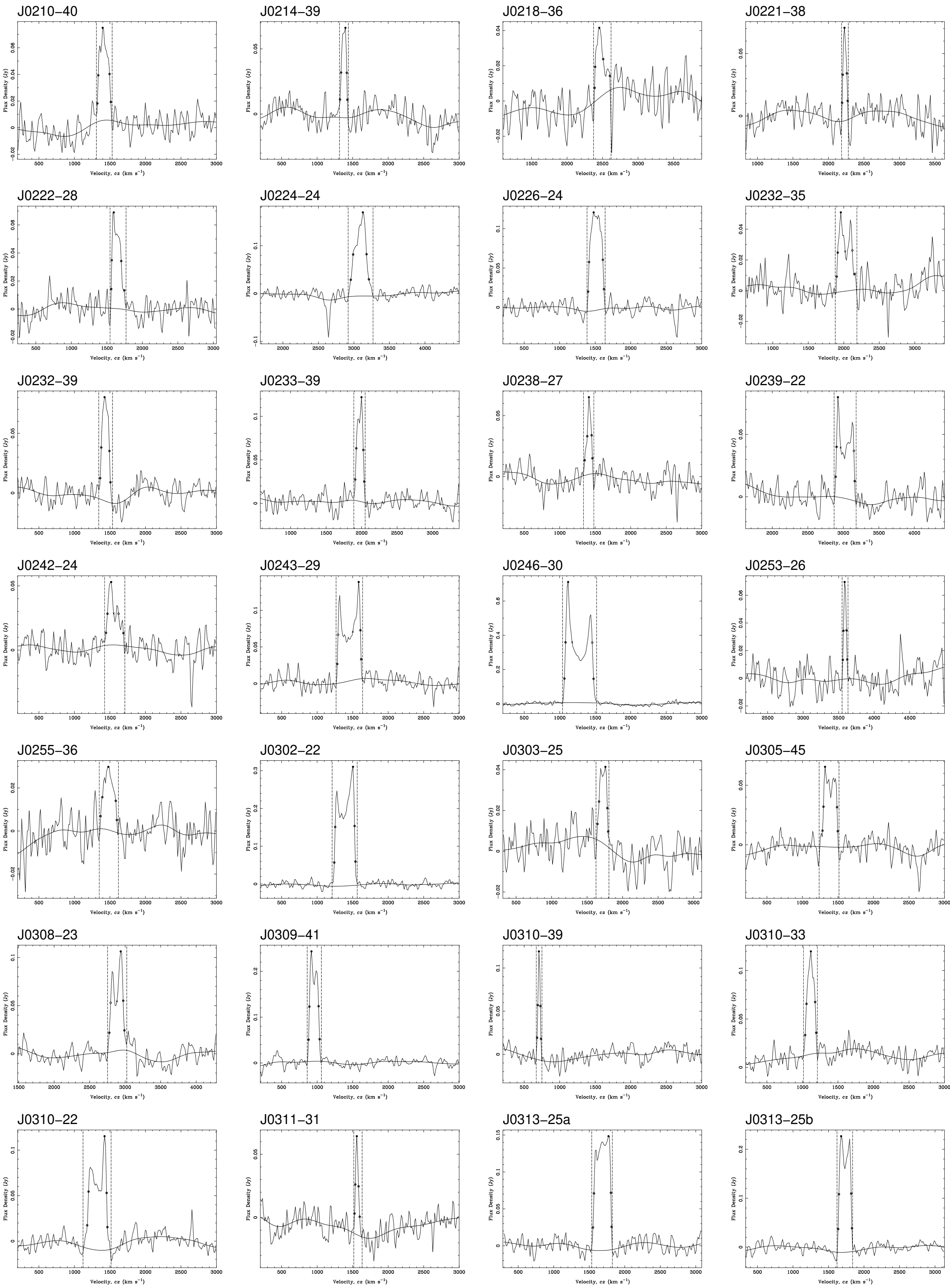
J0210−40
J0214−39
J0218−36
J0221−38
J0222−28
J0224−24
J0226−24
J0232−35
J0232−39
J0233−39
J0238−27
J0239−22
J0242−24
J0243−29
J0246−30
J0253−26
J0255−36
J0302−22
J0303−25
J0305−45
J0308−23
J0309−41
J0310−39
J0310−33
J0310−22
J0311−31
J0313−25a
J0313−25b

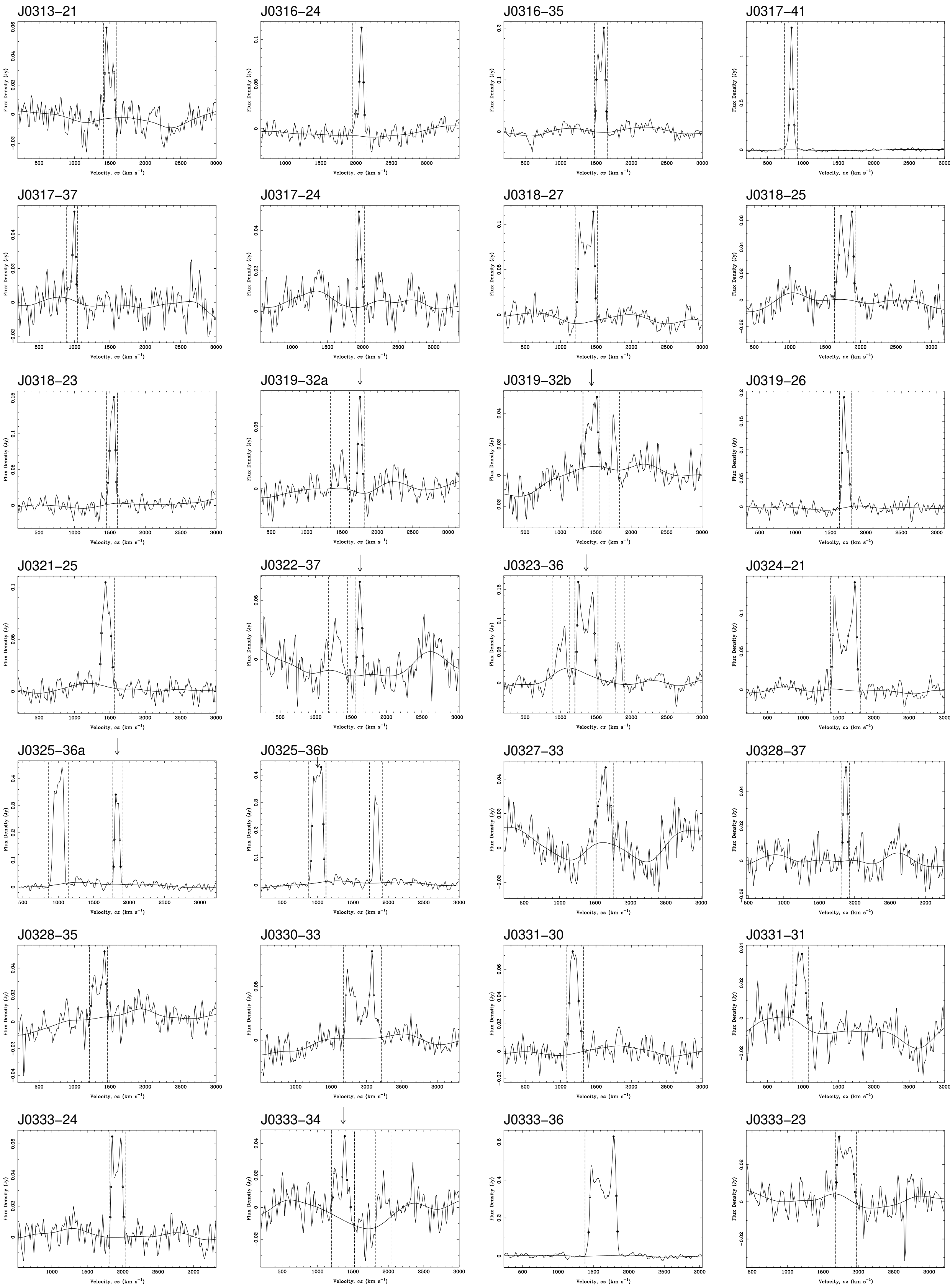
J0313−21
J0316−24
J0316−35
J0317−41
J0317−37
J0317−24
J0318−27
J0318−25
J0318−23
J0319−32a
J0319−32b
J0319−26
J0321−25
J0322−37
J0323−36
J0324−21
J0325−36a
J0325−36b
J0327−33
J0328−37
J0328−35
J0330−33
J0331−30
J0331−31
J0333−24
J0333−34
J0333−36
J0333−23
Flux Density (Jy)
Velocity, cz (km s−1)

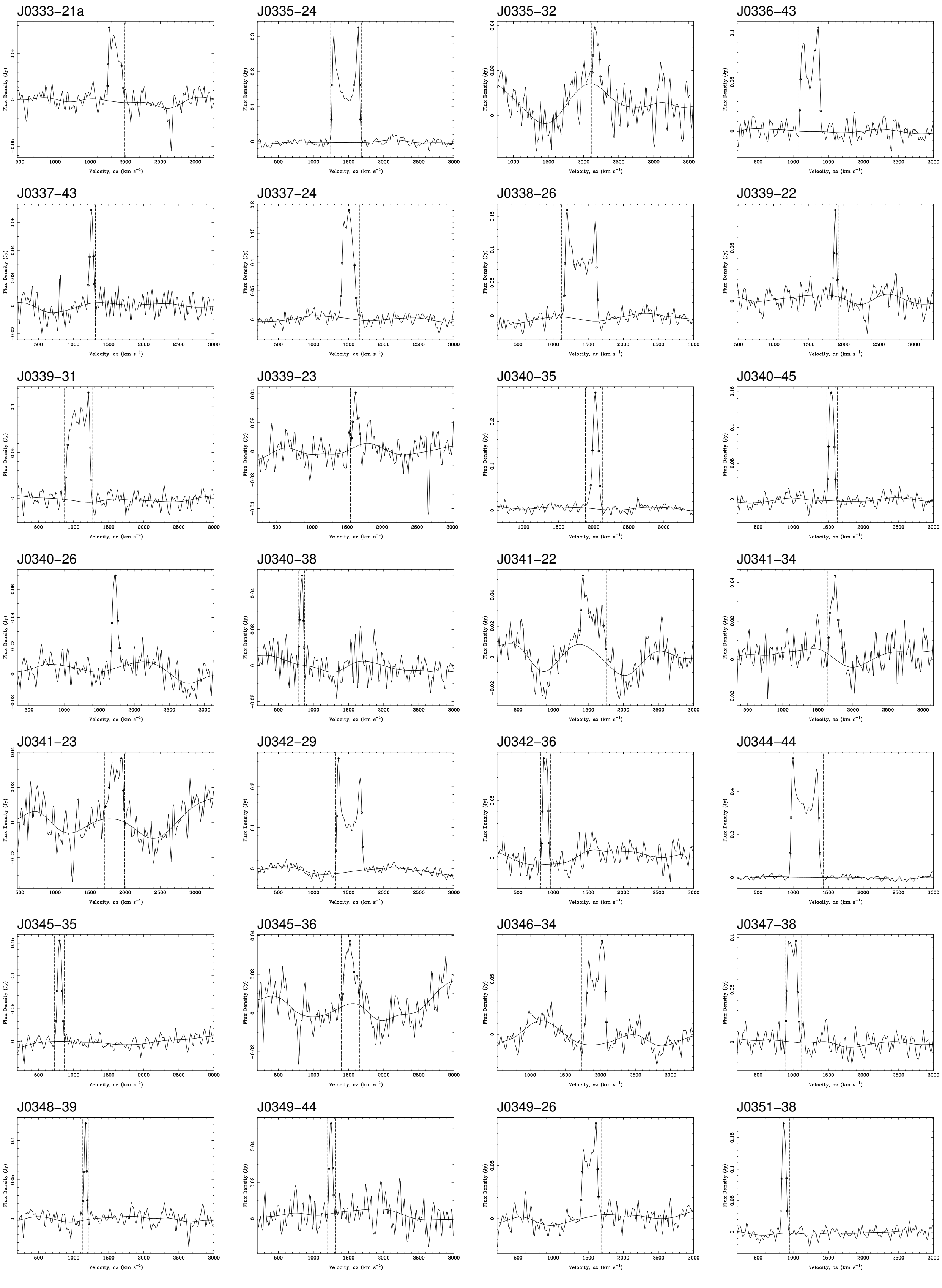

J0333−21a
J0335−24
J0335−32
J0336−43
J0337−43
J0337−24
J0338−26
J0339−22
J0339−31
J0339−23
J0340−35
J0340−45
J0340−26
J0340−38
J0341−22
J0341−34
J0341−23
J0342−29
J0342−36
J0344−44
J0345−35
J0345−36
J0346−34
J0347−38
J0348−39
J0349−44
J0349−26
J0351−38

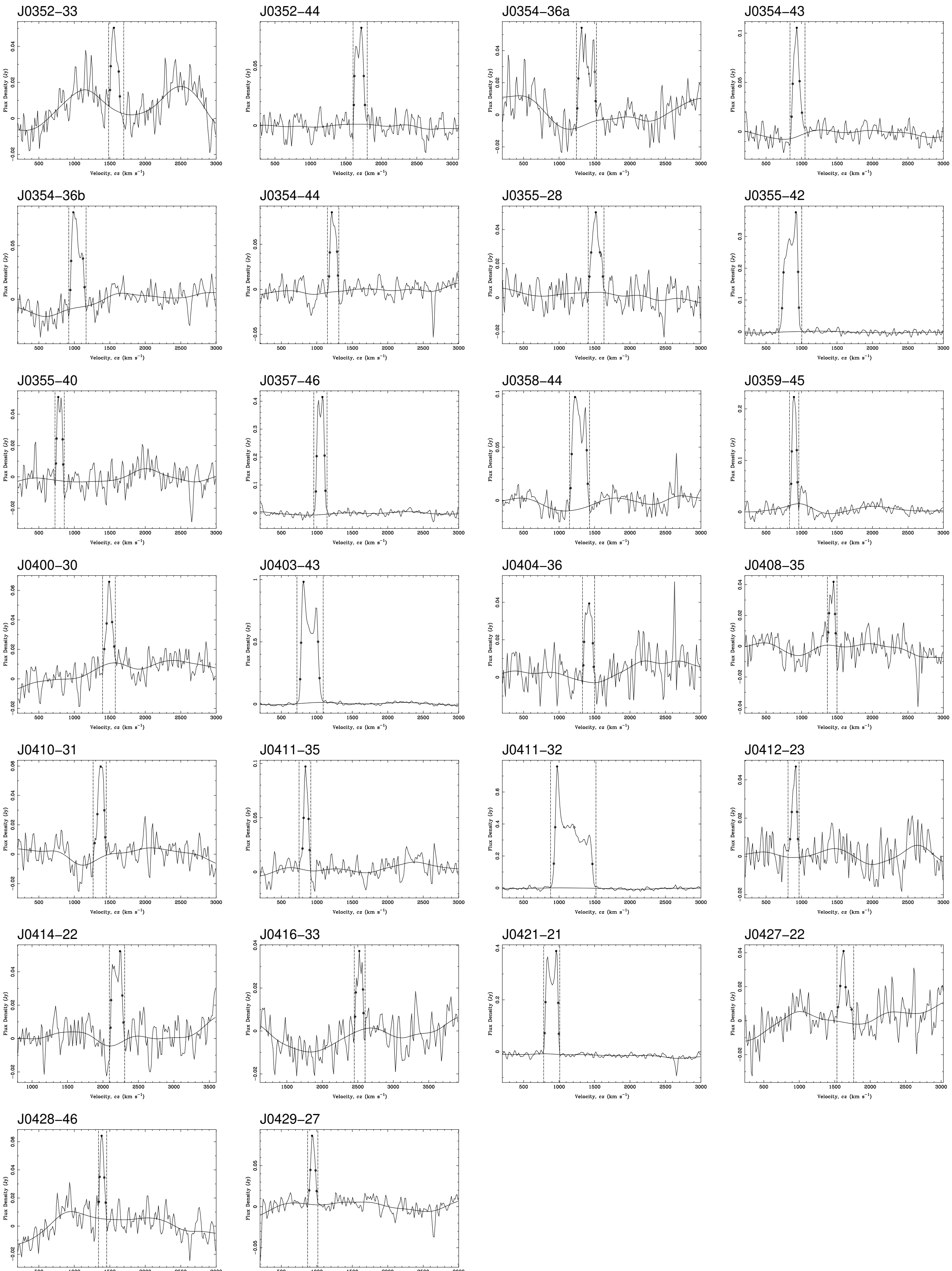
J0352−33
J0352−44
J0354−36a
J0354−43
J0354−36b
J0354−44
J0355−28
J0355−42
J0355−40
J0357−46
J0358−44
J0359−45
J0400−30
J0403−43
J0404−36
J0408−35
J0410−31
J0411−35
J0411−32
J0412−23
J0414−22
J0416−33
J0421−21
J0427−22
J0428−46
J0429−27
Flux Density (Jy)
Velocity, cz (km s−1)